

# Chemical Stabilization of 1T' Phase Transition Metal Dichalcogenides with Giant Optical Kerr Nonlinearity

Sherman J. R. Tan,<sup>†,‡,∇</sup> Ibrahim Abdelwahab,<sup>†,‡,∇</sup> Zijing Ding,<sup>§,⊥</sup> Xiaoxu Zhao,<sup>†,‡</sup> Tieshan Yang,<sup>||</sup> Gabriel Z. J. Loke,<sup>⊥</sup> Han Lin,<sup>||</sup> Ivan Verzhbitskiy,<sup>⊥,⊗</sup> Sock Mui Poh,<sup>†,‡</sup> Hai Xu,<sup>†</sup> Chang Tai Nai,<sup>†</sup> Wu Zhou,<sup>#</sup> Goki Eda,<sup>†,⊥,⊗</sup> Baohua Jia,<sup>||</sup> and Kian Ping Loh<sup>\*,†,⊗,||</sup>

<sup>†</sup>Department of Chemistry, National University of Singapore, Singapore 117543, Singapore

<sup>‡</sup>NUS Graduate School for Integrative Sciences and Engineering, Centre for Life Sciences, National University of Singapore, #05-01, 28 Medical Drive, Singapore 117456, Singapore

<sup>§</sup>SZU-NUS Collaborative Innovation Center for Optoelectronic Science & Technology, Key Laboratory of Optoelectronic Devices and Systems of Ministry of Education and Guangdong Province, College of Optoelectronic Engineering, Shenzhen University, Shenzhen 518060, China

<sup>||</sup>Centre for Micro-Photonics, Faculty of Science Engineering and Technology, Swinburne University of Technology, Hawthorn, Victoria 3122, Australia

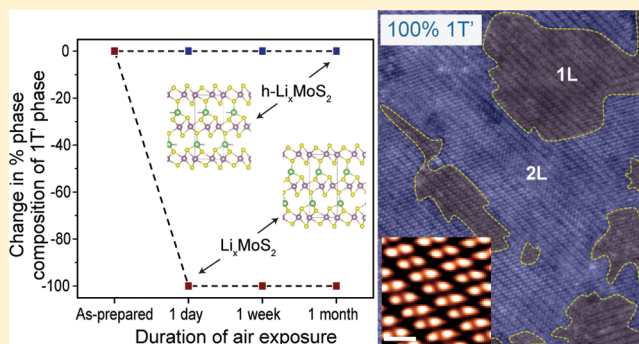
<sup>⊥</sup>Department of Physics, National University of Singapore, Singapore 117551, Singapore

<sup>#</sup>Materials Science & Technology Division, Oak Ridge National Laboratory, Oak Ridge, Tennessee 37831, United States

<sup>⊗</sup>Centre for Advanced 2D Materials and Graphene Research Centre, National University of Singapore, Singapore 117546, Singapore

## Supporting Information

**ABSTRACT:** The 2H-to-1T' phase transition in transition metal dichalcogenides (TMDs) has been exploited to phase-engineer TMDs for applications in which the metallicity of the 1T' phase is beneficial. However, phase-engineered 1T'-TMDs are metastable; thus, stabilization of the 1T' phase remains an important challenge to overcome before its properties can be exploited. Herein, we performed a systematic study of the 2H-to-1T' phase evolution by lithiation in ultrahigh vacuum. We discovered that by hydrogenating the intercalated Li to form lithium hydride (LiH), unprecedented long-term (>3 months) air stability of the 1T' phase can be achieved. Most importantly, this passivation method has wide applicability for other alkali metals and TMDs. Density functional theory calculations reveal that LiH is a good electron donor and stabilizes the 1T' phase against 2H conversion, aided by the formation of a greatly enhanced interlayer dipole–dipole interaction. Nonlinear optical studies reveal that air-stable 1T'-TMDs exhibit much stronger optical Kerr nonlinearity and higher optical transparency than the 2H phase, which is promising for nonlinear photonic applications.



## INTRODUCTION

Transition metal dichalcogenides (TMDs) represent a large family of layered materials with  $\text{MX}_2$  stoichiometry, where M is a transition metal and X is a chalcogen. The lack of an inversion symmetry in monolayer or odd-layered TMDs enables the exploitation of second order effects such as second and third harmonic generation. Giant optical nonlinearity in 2D TMDs is ascribed to its 2D confinement, strong enhancement of light-matter interactions by excitonic effects and band edge resonances. Depending on the electron filling in the valence  $d$ -orbitals of the transition metal, TMDs can manifest in different polymorphs which exhibit a diverse range of electronic and optical properties. For example, group VI TMDs such as  $\text{MoS}_2$  and  $\text{WSe}_2$  exist in the stable semiconducting 2H phase,

while the distorted, metallic 1T (1T') phase is unstable at ambient conditions. The 1T' phase has been recently predicted to exhibit interesting phenomena, such as quantum spin Hall effect,<sup>1</sup> Weyl semimetal,<sup>2,3</sup> dipolar ferroelectricity,<sup>4</sup> and charge density wave formation,<sup>5</sup> and plays a pivotal role in the fabrication of low-resistance contacts for 2D TMD transistor devices.<sup>6–8</sup> While much attention has been focused on studying the nonlinear optical properties of the 2H-semiconducting phase of  $\text{MoS}_2$ , little work has been carried out on the 1T' phase, which are expected to possess interesting optical

Received: December 23, 2016

Published: January 23, 2017

properties due to the low symmetry of the distorted phase and its anisotropic optical properties.

Several methods have been employed to induce 2H-to-1T' phase transition in TMDs, including intercalation with alkali metals,<sup>9–11</sup> electron beam irradiation,<sup>12,13</sup> mechanical strain,<sup>14</sup> and plasmonic excitation.<sup>15</sup> The weak van der Waals bonding between the TMD layers allows alkali metal ions to intercalate, forming ternary compounds which are highly anisotropic and possessing pseudo two-dimensional properties.<sup>16,17</sup> The 1T' domains are usually found in low concentrations with respect to the 2H phase, especially after air-exposure,<sup>18</sup> mild annealing, or aging.<sup>19,20</sup> Lacking a method to stabilize the 1T' phases against 2H conversion means that many 1T'-associated properties are short-lived in air, which prevents detailed investigation into the intriguing properties of this phase. It is therefore essential to develop a phase engineering strategy which not only achieves complete phase conversion, but also stabilizes the 1T' phase against degradation in air.

Herein, we report an effective phase engineering method which can achieve complete 2H-to-1T' phase conversion in TMDs. Most importantly, the 1T' phase can be stabilized against conversion to the 2H phase for extended periods of time in air. Our method involves intercalating MoS<sub>2</sub>, a prototypical TMD, by lithium atoms generated from a standard getter source, followed by thermally activated hydrogenation of the intercalated Li to form LiH. The ability to achieve stable and homogeneous 1T' phase in TMDs allows us to study its nonlinear optical properties as a function of laser power in air, where giant optical Kerr nonlinearities in 1T'-MoS<sub>2</sub> and 1T'-WS<sub>2</sub> are discovered.

## RESULTS

Lithium is evaporated on few-layered MoS<sub>2</sub> using a SAES Li getter source (Supporting Information (SI), Figure S1). Evaporated lithium atoms are highly diffusive and can intercalate 2D MoS<sub>2</sub> as well as 3D MoS<sub>2</sub> crystals up to a depth of ~50 nm, as is confirmed by secondary ion mass spectrometry (SI, Figure S2). As shown in Figure 1a, upon Li intercalation, the Mo 3d core level peaks chemically shift such that its binding energies are 1.0 eV lower than that of pristine 2H samples, which is assigned to the 1T' phase of MoS<sub>2</sub> (confirmed by Raman and TEM discussed later). The decrease in binding energy is due to the chemical reduction of Mo from the +4 to the +3 oxidation state.<sup>7,9</sup> The Li evaporation flux can be controlled readily, thus allowing the staged phase transformation of Li<sub>x</sub>MoS<sub>2</sub> to be captured using *in situ* X-ray photoemission spectroscopy (XPS), as shown in the inset of Figure 1a. The first order 2H-to-1T' phase transformation occurs at  $x > 0.2$ . A full 1T' phase conversion can be obtained at higher stoichiometric ratio of Li ( $x > 1.2$ ), as evidenced by the complete reduction of Mo<sup>4+</sup> to Mo<sup>3+</sup> in the XPS spectra. There is no significant change in the full width at half-maximum (fwhm) of Mo 3d core level peaks, suggesting that the crystallinity of the sample is preserved. This is consistent with our *ex situ* X-ray diffraction (XRD) results which also indicate no broadening in the fwhm of the diffraction peaks (SI, Figure S3), confirming that the dry intercalation method here yields high-quality Li<sub>x</sub>MoS<sub>2</sub> crystals. The obtained Li<sub>x</sub>MoS<sub>2</sub> is stabilized by annealing in a hydrogen atmosphere at 473 K (Figure 1b). Upon hydrogenation, the binding energies and peak areas of the Mo 3d and S 2p core level peaks do not change, indicating that hydrogenation does not affect the phase composition of Li<sub>x</sub>MoS<sub>2</sub>. However, the binding energy of the Li

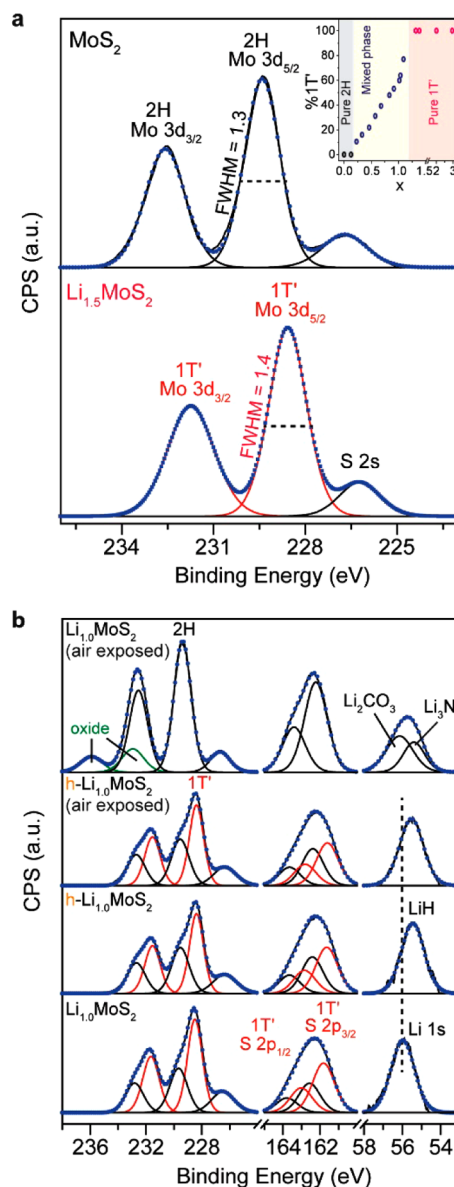


**Figure 1.** *In situ* XPS of h-Li<sub>x</sub>MoS<sub>2</sub>. (a) XPS spectra showing Mo 3d core levels of pristine 2H-MoS<sub>2</sub> (top) and fully converted 1T'-Li<sub>1.5</sub>MoS<sub>2</sub> (bottom). The FWHM values of the Mo 3d<sub>5/2</sub> core levels are indicated next to the peaks. Inset shows the plot of 1T' phase composition against amount of Li ( $x$ ) in Li<sub>x</sub>MoS<sub>2</sub>. (b) XPS spectra showing the Mo 3d, S 2p, and Li 1s core levels of hydrogenated (h-Li<sub>1.0</sub>MoS<sub>2</sub>) and non-hydrogenated (Li<sub>1.0</sub>MoS<sub>2</sub>) samples before and after air exposure, taken with a spot size of 5 mm. Mo 3d and S 2p core level peaks associated with 1T' (2H) phase are labeled and colored in red (black).

1s core level decreases by 0.5 eV to 55.5 eV, which is consistent with the formation of LiH.<sup>21</sup> Additionally, we observe the Li-H stretching mode in the high-resolution electron energy loss (HREELS) spectra (SI, Figure S4). In order to test the stability of h-Li<sub>x</sub>MoS<sub>2</sub>, we exposed the sample to air. Remarkably, ambient exposure did not produce any change in the Mo 3d and S 2p core level peaks associated with the 1T' phase.

Lithium is known to be highly susceptible to hydrolysis and nitrogeneration in air;<sup>22–24</sup> however, the Li 1s core level peak of the h-Li<sub>x</sub>MoS<sub>2</sub> peak did not change upon ambient exposure. Control experiment shows that without the hydrogenation-stabilization step, air-exposed Li reacts to form Li<sub>2</sub>CO<sub>3</sub> and

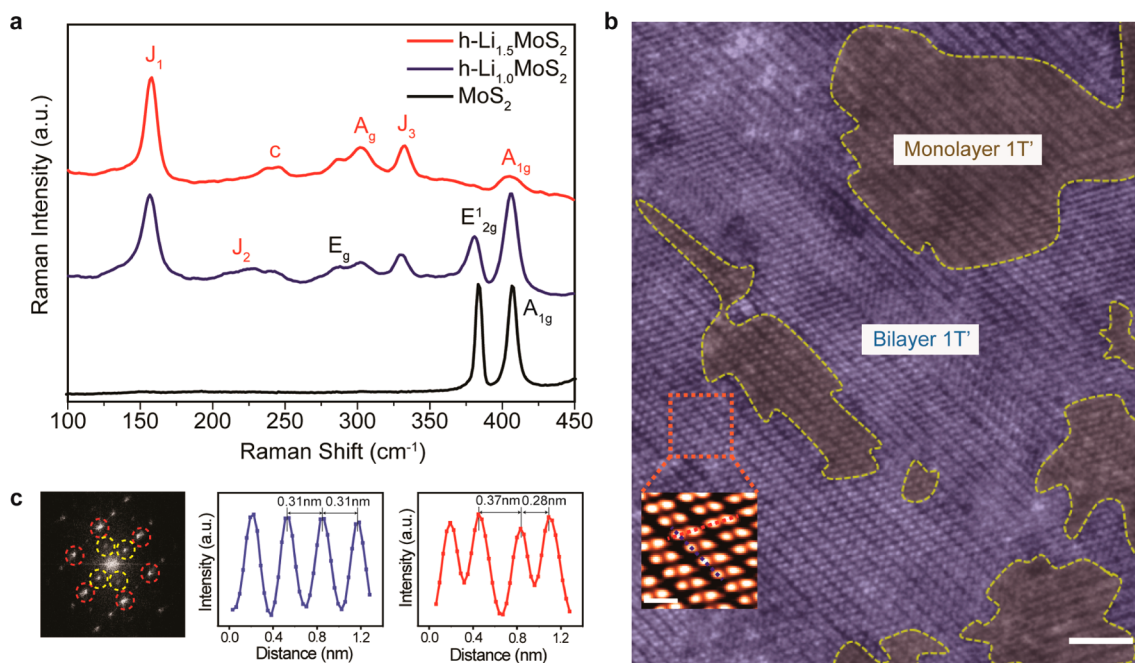


**Figure 2.** *Ex situ* characterizations of  $h\text{-Li}_x\text{MoS}_2$ . (a) Raman spectra of pristine 2H-MoS<sub>2</sub>, mixed 2H/1T' phase  $h\text{-Li}_{1.0}\text{MoS}_2$ , and pure 1T' phase  $h\text{-Li}_{1.5}\text{MoS}_2$  taken with 532 nm laser. Raman modes unique to the 1T' phase are labeled in red. (b) Annular dark-field scanning transmission electron microscopy image of monolayer and bilayer  $h\text{-Li}_x\text{MoS}_2$  regions with false color to differentiate the different layers. Inset shows the magnified filtered image of 1T' phase region indicated by the dotted orange box. Scale bars for image and inset are 2.5 and 0.5 nm, respectively. (c) Fast Fourier transform pattern of (b) (left panel) and intensity profiles (middle and right panels) of blue and red lines indicated by inset of (b) showing alternating atomic spacing along one direction with spacing corresponding to zigzag Mo chains from 1T'-MoS<sub>2</sub>.

$\text{Li}_3\text{N}^{25}$  immediately, and  $\text{Li}_x\text{MoS}_2$  reverts to the 2H phase (Figure 1b). Consistent with our XPS results, *ex situ* Raman spectroscopy confirms a full 2H-to-1T' phase conversion at higher stoichiometric ratios of Li. 2H-MoS<sub>2</sub> can be unambiguously identified by the zone-center Raman modes at 383 cm<sup>-1</sup> ( $E_{2g}^1$  mode) and 409 cm<sup>-1</sup> ( $A_{1g}$  mode).<sup>26,27</sup> In particular, the  $E_{2g}^1$  mode is unique to the 2H phase and absent in the 1T'-MoS<sub>2</sub>; the absence of the  $E_{2g}^1$  mode is observed in the  $h\text{-Li}_{1.50}\text{MoS}_2$  sample, indicating a full 2H-to-1T' phase conversion (Figure 2a). In addition to the signature Raman peaks of 1T'-MoS<sub>2</sub> at 158, 218, 301, and 334 cm<sup>-1</sup>, which correspond to the  $J_1$ ,  $J_2$ ,  $A_g$ , and  $J_3$  peaks, respectively,<sup>28</sup> a peak labeled "c", corresponding to the out-of-plane Li-S Raman mode of Li-intercalated MoS<sub>2</sub>,<sup>29</sup> is also observed. Interestingly, the intensity of the  $J_2$  peak is very weak in the mixed phase sample ( $h\text{-Li}_{1.0}\text{MoS}_2$ ) and disappears in the pure  $h\text{-Li}_{1.5}\text{MoS}_2$ .  $J_2$  is assigned to the longitudinal acoustic mode at the M-point and is only allowed by disorder; thus, it was previously observed in solution-phase chemical exfoliated samples and MoS<sub>2</sub> nanoparticles with fullerene-like geometry.<sup>26,30</sup> At the intermediate stage before full 1T' coverage is attained ( $\text{Li}_{0.2 < x < 1.2}\text{MoS}_2$ ), a mixture of 2H and 1T' polytypes, joined by disordered grain boundaries, coexists in the MoS<sub>2</sub> film. The defect-related  $J_2$  peak may emanate from the grain boundary regions, since this peak vanishes when a full 1T' phase is developed at full lithiation ( $x \approx 1.2$ ).

Scanning transmission electron microscopy (STEM) images of the  $h\text{-Li}_x\text{MoS}_2$  sample reveal the presence of alternating one-dimensional zigzag stripes on the basal plane, with measured Mo-Mo distances of 0.37 and 0.28 nm, corresponding to the 1T' phase unit cells with  $2 \times 1$  superstructure<sup>31</sup> (Figure 2b), which is confirmed also by the presence of the half-order superstructure spots in the FFT diffraction image shown in

Figure 2c (0.17 Å<sup>-1</sup>  $d$ -spacing, highlighted as yellow circles). The increased stability of our  $h\text{-Li}_x\text{MoS}_2$  (1T') sample is also reflected in the much higher 1T'-to-2H phase conversion temperature, determined using *in situ* XPS. It was observed that the 1T'-to-2H phase transition proceeds only above 673 K, which is markedly increased compared to 1T'-MoS<sub>2</sub> samples (373 K) prepared by solution-phase method.<sup>9</sup> The increased thermal stability of our  $h\text{-Li}_x\text{MoS}_2$  samples is useful because it will facilitate the subsequent device fabrication process, which often requires post-annealing treatment.

Despite subjecting the  $h\text{-Li}_x\text{MoS}_2$  samples to multiple characterizations over an extended period in air, we find that the 1T' phase remains relatively stable, as judged by its steady spectroscopic signatures in Raman, XRD, and XPS when sampled periodically over time (Figure 3a). Raman spectra of  $h\text{-Li}_x\text{MoS}_2$  aged for three months in air show no discernible degradation of the 1T'-related peaks (Figure 3b). This is in stark contrast to the samples which are not hydrogenated, for which the signal decays rapidly within a day. One possible reason is the rapid oxidation and nitrogenation of lithium in air<sup>22</sup> (Figure 1b), which reduced its electron donating ability. The 2H-to-1T' phase change has an electronic origin. The formation of the  $d^3$  configuration after electron transfer to the Mo 4d orbitals destabilizes the trigonal prismatic structure in the 2H phase in favor of the octahedral structure adopted by the 1T' phase.<sup>32</sup> Intercalated Li atoms act as electron donors, therefore, the reduction in their electron donating ability after exposure to air will destabilize the 1T' phase against the 2H phase.

One question is whether the stabilization achieved by the formation of alkali metal hydride is generic for other combinations of layered 2D materials and alkali metal intercalants. As a further proof of principle, we demonstrate

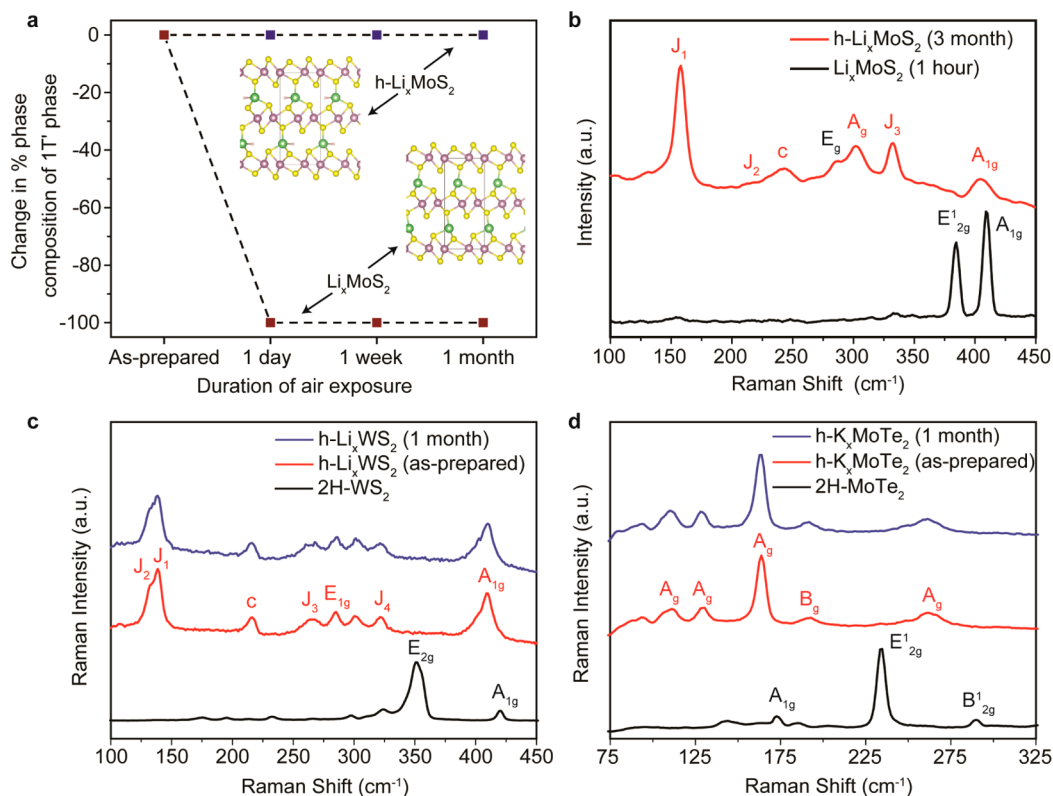


**Figure 3.** Degradation rate and long-term stability investigation of stabilized alkali metal intercalated TMDs. (a) Degradation of  $\text{h-Li}_x\text{MoS}_2$  in ambient conditions, investigated by the change in %  $1\text{T}'$  phase composition as determined by XPS. (b) Raman spectra of  $\text{h-Li}_x\text{MoS}_2$  and  $\text{Li}_x\text{MoS}_2$ . Duration of air exposures are indicated in brackets next to their label. Raman modes unique to the  $1\text{T}'$  phase are labeled in red. (c) Raman spectra of pristine  $2\text{H-WS}_2$  (black) and hydrogenated lithium-intercalated  $\text{WS}_2$  ( $\text{h-Li}_x\text{WS}_2$ ) as-prepared (red) and after ambient exposure for 1 month (blue) showing the persistence of signature  $1\text{T}'$  peaks. (d) Raman spectra of pristine  $2\text{H-MoTe}_2$  (black) and potassium hydride-intercalated  $\text{MoTe}_2$  ( $\text{h-K}_x\text{MoTe}_2$ ) as-prepared (red) and after ambient exposure for 1 month (blue) showing the persistence of signature  $1\text{T}'$  peaks. All peaks originating from  $1\text{T}'$  ( $2\text{H}$ ) phase are labeled in red (black) for clarity.

that lithium hydride-intercalated  $\text{WS}_2$  ( $\text{h-Li}_x\text{WS}_2$ ) and potassium hydride-intercalated  $\text{MoTe}_2$  ( $\text{h-K}_x\text{MoTe}_2$ ) undergo complete  $2\text{H}$ -to- $1\text{T}'$  phase transformation and are stabilized against  $2\text{H}$  phase conversion, similar to  $\text{h-Li}_x\text{MoS}_2$  demonstrated above (other combinations can be found in SI, Figures S5–S7). As shown in Figure 3c, as-exfoliated  $\text{WS}_2$  displayed two characteristic  $2\text{H}$  phase Raman peaks at  $352$  and  $420\text{ cm}^{-1}$ , corresponding to the in-plane  $\text{E}_{2g}$  and out-of-plane  $\text{A}_{1g}$  modes, respectively. The other weaker peaks belong to the second order Raman modes.<sup>33</sup> Upon Li intercalation and formation of the hydride, we observed the disappearance of the  $2\text{H}$  phase Raman peaks and the emergence of peaks at  $132$ ,  $139$ ,  $265$ ,  $285$ ,  $321$ , and  $409\text{ cm}^{-1}$ , corresponding to the theoretically predicted  $\text{J}_2$ ,  $\text{J}_1$ ,  $\text{J}_3$ ,  $\text{E}_{1g}$ ,  $\text{J}_4$ , and  $\text{A}_{1g}$  modes of  $1\text{T}'\text{-WS}_2$ , respectively.<sup>34</sup> To the best of our knowledge this is the first complete experimental Raman assignment of  $1\text{T}'\text{-WS}_2$ , which is made possible by the enhanced stabilization of the  $1\text{T}'$  phases by the passivation method reported here. Remarkably, the  $1\text{T}'$  phase of  $\text{WS}_2$  displays high ambient stability (at least 1 month) using our hydrogenation–stabilization method, which attests to the usefulness of the alkali metal hydride method in stabilizing metastable  $1\text{T}'\text{-TMDs}$ .

The stability of the alkali metal hydrides is known to decrease with an increase in the ionic radius of the metal.<sup>35</sup> The strongest lattice is formed by Li cations and hydrides, which have the most compatible ion sizes. This trend explains the increasing reactivity of the hydrides from  $\text{NaH}$  to  $\text{CsH}$ , whereas  $\text{LiH}$  is more inert. Due to the much higher reactivity of K,

neither the stability, nor the existence of the  $1\text{T}'$  phase in K-intercalated TMDs has been reported previously. Zheng et al. attempted the chemical intercalation of  $\text{MoS}_2$  using potassium naphthalenide, and discovered that the much higher reactivity of potassium causes the intercalant to be hydrated rapidly in air.<sup>36</sup> As shown in Figure 3d, the  $1\text{T}'$  phase is stabilized in potassium hydride-intercalated  $\text{MoTe}_2$  ( $\text{h-K}_x\text{MoTe}_2$ ). Our as-exfoliated  $2\text{H-MoTe}_2$  samples displayed three characteristic Raman modes of the  $2\text{H}$  phase at  $173$ ,  $234$ , and  $290\text{ cm}^{-1}$ , corresponding to the  $\text{A}_{1g}$ ,  $\text{E}^1_{2g}$ , and  $\text{B}^1_{2g}$  modes, respectively.<sup>37</sup> The weaker peaks belong to the second order Raman modes of  $2\text{H-MoTe}_2$ .<sup>38</sup> After K intercalation and hydride formation, we observed the disappearance of the  $2\text{H}$  peaks and emergence of  $1\text{T}'$ -associated  $\text{MoTe}_2$  Raman modes<sup>39</sup> at  $111$ ,  $129$ ,  $164$ ,  $193$ , and  $262\text{ cm}^{-1}$ , which remained unchanged in intensities even after 1 month of ambient exposure.

Compared to the laser-induced generation of Te defects in  $\text{MoTe}_2$  for engineering  $2\text{H}$ -to- $1\text{T}'$  phase conversion,<sup>40</sup> the in situ alkali metal intercalation method is advantageous because it does not rely on defect generation and can be scaled up over the entire surface of the TMDs to obtain full  $1\text{T}'$  phase conversion. The generic applicability of this stabilization method is highly significant because it paves the way for fabricating stable  $2\text{D}$  to  $3\text{D}$  alkali metal hydride-intercalated TMDs, thus opening opportunities to examine air-stable devices.

The increased stability of the  $1\text{T}'$  phase in  $\text{LiH}$ -intercalated  $\text{MoS}_2$  has various origins. First, the formation of lithium

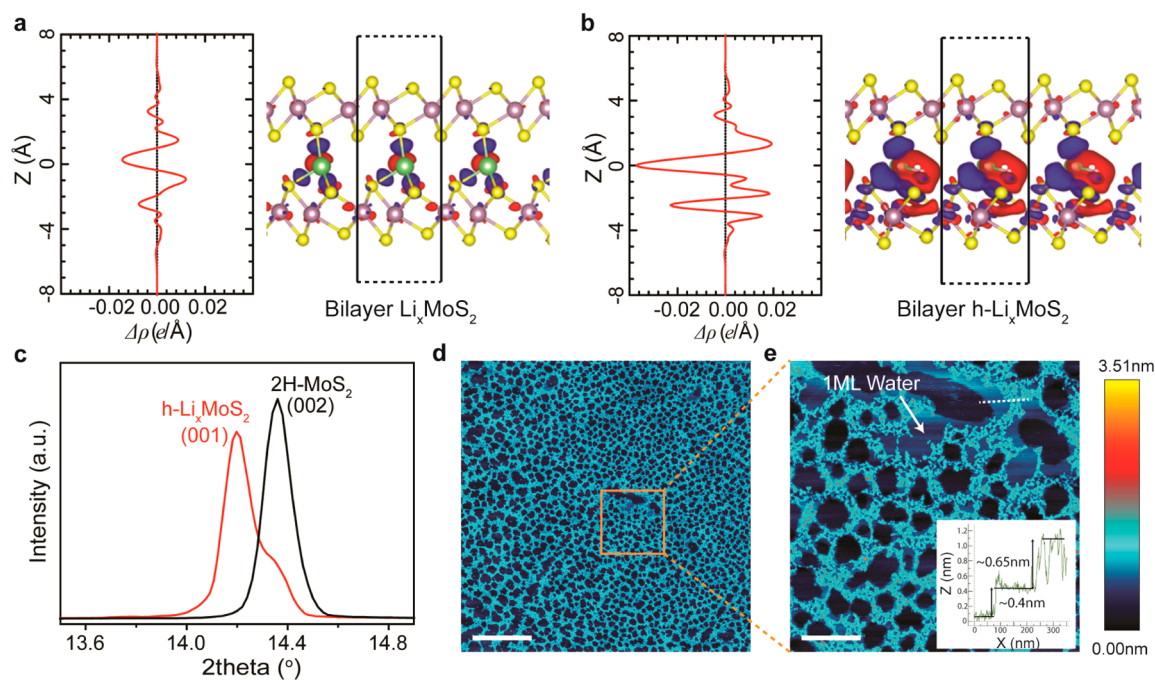


**Figure 4.** Electronic and steric stabilization of  $h\text{-Li}_x\text{MoS}_2$ . (a,b) DFT-calculated differential charge density after intercalation of Li (a) and LiH (b) into bilayer  $1T'\text{-MoS}_2$ . Plane-averaged differential charge density ( $\Delta\rho(z)$ ) plots are shown in the left panels of the region marked by a black box of the isosurface side-view profile at  $0.02 \text{ \AA}^{-3}$  in the right panels. The black dashed lines refer to an interface with vacuum. The red (blue) color of the isosurface plots denotes loss (accumulation) of electrons in the system. (c) Powder XRD spectra of pristine  $2\text{H-MoS}_2$  (black) and  $h\text{-Li}_x\text{MoS}_2$  (red) of the (002) plane region. (d,e) NC-AFM images of surface exfoliated  $h\text{-Li}_x\text{MoS}_2$ . Large-scale topography image is shown in (d), and the zoomed-in region marked by the orange box is shown in (e), together with the height profile of water (1 monolayer) and aggregated Li clusters along the white dotted line. Scale bars for the images are  $1.9 \mu\text{m}$  and  $400 \text{ nm}$ , respectively.

hydride passivates the Li from reacting with air (78% nitrogen) to form  $\text{Li}_3\text{N}$ . The heat of reaction for  $\text{LiH(s)}$  and  $\text{N}_2(\text{g})$  to form  $\text{Li}_3\text{N}$  is endothermic ( $+41 \text{ kJ/mol}$ ), whereas that of  $\text{Li(s)}$  and  $\text{N}_2(\text{g})$  to give the same is exothermic ( $-55 \text{ kJ/mol}$ ); LiH also is less reactive with water compared to Li (see reaction enthalpies in SI, Table S1). Second, LiH can act as a good Lewis base. To understand the role of the LiH intercalant in stabilizing the  $1T'\text{-MoS}_2$ , we calculate the differential charge density (DCD),  $\Delta\rho(r)$ , of  $\text{Li}_x\text{MoS}_2$  and  $h\text{-Li}_x\text{MoS}_2$  (Figure 4a,b). The model is based on a  $1 \times 2 \times 2$  supercell of  $\text{Li}_{0.5}\text{MoS}_2$  constrained by AB-stacked  $2\text{H-MoS}_2$  with the lattice parameters  $a = 3.18 \text{ \AA}$  and  $c = 6.24 \text{ \AA}$ , as determined from experimental XRD and STEM data of our samples. The energetically optimized configuration of intercalated LiH (structure can be found in the insets of Figure 3a) has a binding energy of  $0.24 \text{ eV}$  on the  $\text{MoS}_2$  layers. The magnitude of this binding energy is similar to a hydrogen bond, implying facile intercalation and de-intercalation. To quantify the amount of charge transfer from LiH to  $\text{MoS}_2$ , we calculate the plane-averaged DCD along the direction normal to the surface by integrating  $\Delta\rho(r)$  within the  $x\text{-}y$  plane. The excess electrons transferred from lithium atoms to  $\text{MoS}_2$  is about  $0.818e$  per lithium atom ( $0.41e$  per  $\text{MoS}_2$  unit cell); however, it increases to  $0.879e$  per lithium hydride molecule upon the formation of LiH ( $0.44e$  per  $\text{MoS}_2$  unit cell). These results imply that LiH can act as an effective electron donor, and is capable of inducing  $2\text{H-to-}1T'$  phase transition in  $\text{MoS}_2$ . The DFT calculations also reveal a significant charge redistribution induced by the relatively large dipole moment of LiH, especially in between the  $\text{MoS}_2$  layers, as shown by the isosurface plots. The bond angle of  $\text{Li-H-Li}$  is about  $83^\circ$ , and the dipole is tilted with respect to the  $\text{MoS}_2$  plane. Due to the large

polarized electron cloud of LiH, the charge transfer to the top and bottom  $\text{MoS}_2$  layers is nonequivalent, leading to charge polarization between the top and bottom  $\text{MoS}_2$  plane (Figure 4a,b). The increased free carrier density in  $\text{MoS}_2$  layers upon charge transfer allows creation of image dipoles for screening the huge dipole of LiH. Consequently, the perpendicular dipole moment generated is  $0.123 \text{ D}$  per unit cell for  $h\text{-Li}_x\text{MoS}_2$ , which is of 2 orders of magnitude larger than that of  $\text{Li}_x\text{MoS}_2$  ( $0.00616 \text{ D}$  per unit cell). The giant increase in dipole-dipole interactions creates a strong intermolecular force which decreases the chemical energy of the system. The enhanced interlayer coupling in  $h\text{-Li}_x\text{MoS}_2$  resulting from the increased dipole-dipole interactions contracts the interlayer distance. This is consistent with XRD results, where we observe only a  $0.14 \text{ \AA}$  increase in the  $c$ -spacing of  $h\text{-Li}_x\text{MoS}_2$  compared to  $2\text{H-MoS}_2$ , following intercalation by LiH, as evidenced by the shift of the (002) peak of  $2\text{H-MoS}_2$  from  $14.4^\circ$  to  $14.2^\circ$  (Figure 4c).

In order to verify whether the sandwich layered structure of  $\text{MoS}_2$  layers protects the LiH intercalant from reacting with the ambient environment, we exfoliated the top layers of  $h\text{-Li}_x\text{MoS}_2$  flakes to expose the inner surface. AFM images of the air-exposed surface showed a reticular network of nanoparticles and liquid films (Figure 4d). In the absence of a protecting  $\text{MoS}_2$  layer, the intercalated LiH undergoes rapid oxidation and hydration (SI, Figure S8). With the encapsulation of the alkali metal hydrides by  $\text{MoS}_2$  layers, LiH intercalated- $\text{MoS}_2$  is highly robust, as judged from the stable  $1T'$  signature in Raman even after 1 day of immersion in water (SI, Figure S9).

In order to investigate the optical properties of  $h\text{-Li}_x\text{MoS}_2$ , we performed spectral measurements using dual microscope set up where the sample was illuminated by a broadband beam via an inverted microscope to characterize the optical transmission

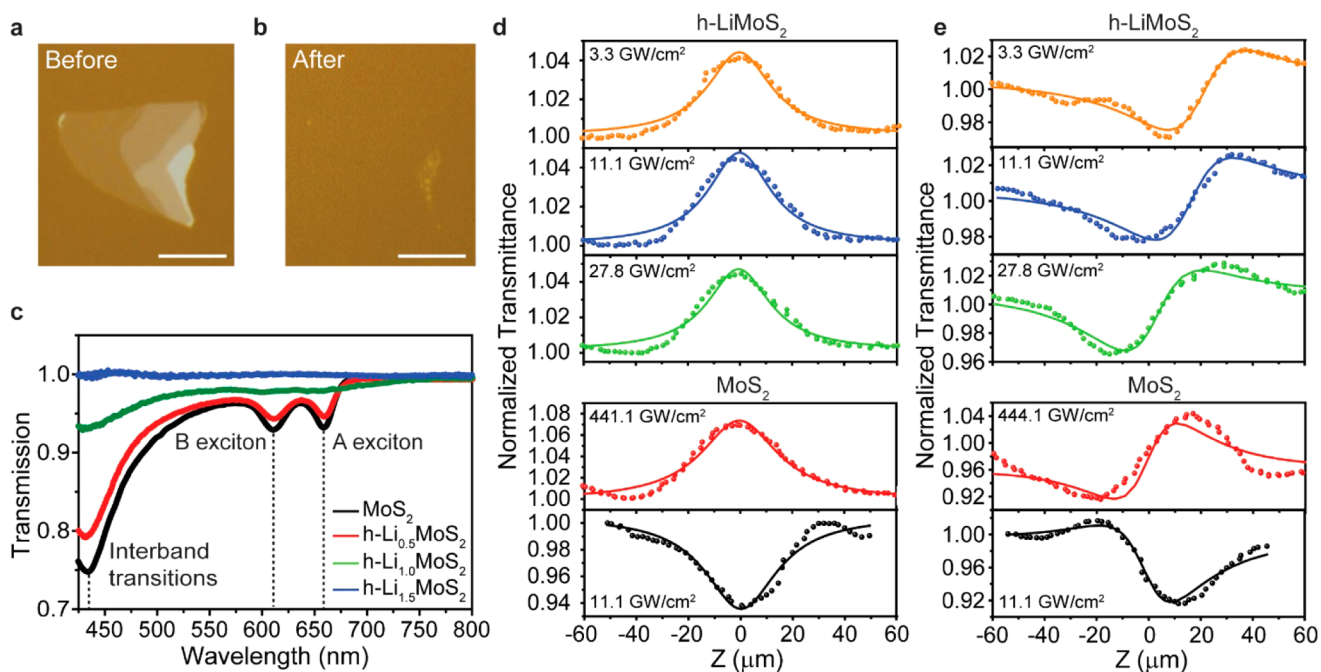


**Figure 5.** Optical characterizations of h-Li<sub>x</sub>MoS<sub>2</sub>. (a,b) Optical images of MoS<sub>2</sub> nanosheets on quartz before (a) and after (b) Li intercalation and chemical stabilization showing transparency of h-Li<sub>x</sub>MoS<sub>2</sub>. Scale bar is 10 μm. (c) Optical transmission spectra of bilayer h-Li<sub>x</sub>MoS<sub>2</sub> flakes with various amounts of Li intercalated. Transmission spectrum of bilayer 2H-MoS<sub>2</sub> is added as a comparison. (d,e) Open (d) and closed (e) aperture Z-scan measurements of h-LiMoS<sub>2</sub> and MoS<sub>2</sub> at different input laser power, indicated at the top left of each curve, showing saturable absorption and self-focusing behavior of h-LiMoS<sub>2</sub> at a lower pumping power.

before and after lithiation. We exfoliated MoS<sub>2</sub> flakes onto quartz substrates and subjected the flakes to UHV Li evaporation and chemical stabilization processes (Figure Sa,b). Figure 5c shows the transmission spectra of h-Li<sub>x</sub>MoS<sub>2</sub> at various Li dosages. As shown, the absorption of pristine 2H-MoS<sub>2</sub> is dominated by three resonance features. The two absorption bands in the region of 575–675 nm are the characteristic direct exciton transitions between the split valence band maxima and conduction band minimum located at the high-symmetry K-point of the Brillouin zone<sup>41</sup> while the strong absorption below 450 nm feature can be attributed to optical transitions in the band nested regions around the  $\Gamma$  point.<sup>42</sup> We observed significant enhancement in transmission with increasing dosage of Li at wavelengths between 425 and 675 nm, as well as a slight decrease in transmission at wavelengths greater than 675 nm when the ratio of Li is  $x = 1$ . Free carrier in the semimetallic 1T' phase screens the electron–hole attraction and weakens excitonic effects; thus, the transmission spectrum becomes relatively flat. Interestingly, we were able to observe an extremely high optical transparency (>99%) in the h-Li<sub>1.5</sub>MoS<sub>2</sub> nanoflakes. As observed in Figure 5b, the thinner nanoflakes, which are 100% 1T' phase, are barely visible in the optical images.

Burstein–Moss type band filling effects is known to broaden optical transparency window in degenerately doped semiconductors, although it is not clear at this stage if it applies due to the semimetallic 1T', which is predicted to have a gap of 0.08 eV.<sup>1</sup> Another factor is due to the upshift of plasma oscillations to the UV range with increasing Li doping in MoS<sub>2</sub>, leading to the reflection of electromagnetic waves with frequencies below the plasma frequency.<sup>43</sup> Furthermore, the broken inversion symmetry in 1T'-TMDs, coupled with carrier-dependent renormalization of electron–hole interactions, can give rise to rich nonlinear optical properties. Therefore, we probed the

nonlinear optical response of 1T'-TMDs by performing open aperture (OA) and closed aperture (CA) Z-scan measurements on few-layered h-LiMoS<sub>2</sub> and h-NaWS<sub>2</sub> flakes using a femtosecond laser (900 nm, 80 MHz, 140 fs). The OA Z-scan measurements for MoS<sub>2</sub> and h-LiMoS<sub>2</sub> are shown in Figure 5d (h-NaWS<sub>2</sub> can be found in SI, Figure S10). We find that h-LiMoS<sub>2</sub> exhibits saturable absorption even at low power level. The extracted nonlinear absorption coefficients,  $\beta$ , are  $-1.182 \times 10^{-4}$ ,  $-3.876 \times 10^{-4}$ , and  $-1.507 \times 10^{-5}$  cm/W, with the corresponding input powers of 3.3, 11.1, and 27.8 GW/cm<sup>2</sup>, respectively. There is no two-photon absorption observed at any power in our experiment for h-LiMoS<sub>2</sub>. In comparison, pristine MoS<sub>2</sub> exhibits obvious two-photon absorption at low power levels (for example at 11.1 GW/cm<sup>2</sup> the  $\beta$  value is  $5.816 \times 10^{-5}$  cm/W) as the laser excitation wavelength sits between the single-photon (1.378 eV) and two-photon (2.756 eV) absorption bands. The threshold power for saturable absorption in pristine MoS<sub>2</sub> is comparatively higher at 444.1 GW/cm<sup>2</sup>, which is 2 orders of magnitude larger than that required for h-LiMoS<sub>2</sub>. This has led to a nonlinear absorption coefficient  $\beta = -1.562 \times 10^{-6}$  cm/W in pristine MoS<sub>2</sub>, which is 2 orders of magnitude lower than that of h-LiMoS<sub>2</sub>. The ease of obtaining saturable absorption implies that upon phase conversion, h-LiMoS<sub>2</sub> has a much higher conduction band electron occupancy, which can explain the high optical transparency in 1T'-TMDs due to Pauli Coulomb blockade. It is known that 1T'-TMDs exhibit metallic character and have lower resistance than the 2H phase. Coupled with its high optical transparency, air-stable 1T'-TMDs have the potential to be used as transparent conductor and saturable absorber for mode-locked and Q-switched ultrafast lasers in ultrafast photonics.

Additionally, as shown in Figure 5e, our CA Z-scan results reveal that h-LiMoS<sub>2</sub> exhibit strong optical Kerr nonlinearity effect, with derived nonlinear refractive indexes,  $n_2$ , of  $2.033 \times$

$10^{-9}$ ,  $5.51 \times 10^{-10}$ , and  $2.897 \times 10^{-10}$   $\text{cm}^2/\text{W}$ , with the corresponding input powers of 3.3, 11.1, and 27.8  $\text{GW}/\text{cm}^2$ , respectively. Typical semiconductor materials such as Si ( $n_2 = 0.5 \times 10^{-13}$   $\text{cm}^2/\text{W}$ ) and GaAs ( $n_2 = 1.5 \times 10^{-13}$   $\text{cm}^2/\text{W}$ ) used in current electronic devices fall short of the required nonlinear refractive index ( $>10^{-10}$   $\text{cm}^2/\text{W}$ ) to produce attractive index change for optical devices.<sup>44</sup> The strong optical Kerr nonlinearity discovered in h-LiMoS<sub>2</sub> and h-NaWS<sub>2</sub>, which outperforms most of the other two-dimensional materials, suggests that air-stable 1T'-TMDs can be potentially used for optical signal modulation in optoelectronic platforms. Furthermore, we observe a valley–peak type curve for h-LiMoS<sub>2</sub> at any input power, while pristine MoS<sub>2</sub> exhibit a peak–valley type curve for most of the power levels (for example at 11.1  $\text{GW}/\text{cm}^2$ ), indicating self-focusing and self-defocusing behaviors, respectively. Only at high input powers (with a threshold at 444.1  $\text{GW}/\text{cm}^2$ ), MoS<sub>2</sub> exhibit peak–valley shapes with a derived threshold nonlinear refractive index,  $n_2$ , of  $3.69 \times 10^{-11}$   $\text{cm}^2/\text{W}$ , which is 2 orders of magnitude lower than that of h-LiMoS<sub>2</sub>. The strong nonlinear optical susceptibilities and switchable self-focusing behavior of air-stable phase-engineered TMDs, together with its low linear absorption loss and nonlinear two-photon absorption loss, open up tremendous possibilities for applications as waveguides and ultrafast switches in integrated photonic circuits.

## CONCLUSION

In summary, we have shown that full 1T' phase can be engendered in MoS<sub>2</sub> by the controlled evaporation of Li in vacuum to produce Li<sub>x</sub>MoS<sub>2</sub> ( $x > 1.2$ ). By exploiting the interlayer diffusivity of hydrogen, the reactivity of intercalated alkali metals in TMDs is reduced by the formation of alkali metal hydride. A synergistic interaction is observed between the host and intercalant: intercalated alkali metal hydrides are good electron donors and stabilize the 1T' phase in air, while the TMDs layers sandwich and protect the alkali metal hydrides from reactive species in the ambient environment. The generic applicability of this method has been verified in other kinds of TMDs (e.g., WS<sub>2</sub> and MoTe<sub>2</sub>) and also with different alkali metal hydrides (e.g., LiH and KH). Giant optical Kerr nonlinearity and higher optical transparency has been observed in 1T'-MoS<sub>2</sub>, where its chemical stability permits high-power laser irradiation. The ability to prepare air-stable, large area, homogeneous 1T' phase of MoS<sub>2</sub> allows the material to be exploited as a nonlinear optical material which can be used as saturable absorber or optical limiters. Finally, the ability to generate in TMD material two phases (e.g., 2H and 1T') with markedly different nonlinear refractive index and extinction coefficient suggests the potential for phase and amplitude modulations, enabling applications in flat lenses.

## ASSOCIATED CONTENT

### Supporting Information

The Supporting Information is available free of charge on the ACS Publications website at DOI: 10.1021/jacs.6b13238.

Experimental details and supporting figures (PDF)

## AUTHOR INFORMATION

### Corresponding Author

\*chmlhkp@nus.edu.sg

### ORCID

Sherman J. R. Tan: 0000-0003-1591-3497

Kian Ping Loh: 0000-0002-1491-743X

### Author Contributions

<sup>†</sup>S.J.R.T. and I.A. contributed equally.

### Notes

The authors declare no competing financial interest.

## ACKNOWLEDGMENTS

K.P.L. is grateful for funding from the National Research Foundation, Prime Minister's Office, Mid-sized Research Centre (CA2DM). This research was also supported in part by the U.S. Department of Energy (DOE), Office of Science, Basic Energy Science, Materials Sciences and Engineering Division (W.Z.), and through a user project at ORNL's Center for Nanophase Materials Sciences (CNMS), which is a DOE Office of Science User Facility. The authors are grateful to Sarkar Soumya (NGS, NUS) for contributing CVD sample for XPS measurements and to Dr. Li Lin Jun (NUS) for discussions. I.A. acknowledges the NUS-Imperial Joint Ph.D. program.

## REFERENCES

- (1) Qian, X.; Liu, J.; Fu, L.; Li, J. *Science* **2014**, *346* (6215), 1344–1347.
- (2) Sun, Y.; Wu, S.-C.; Ali, M. N.; Felser, C.; Yan, B. *Phys. Rev. B: Condens. Matter Mater. Phys.* **2015**, *92* (16), 161107.
- (3) Qi, Y.; Naumov, P. G.; Ali, M. N.; Rajamathi, C. R.; Schnelle, W.; Barkalov, O.; Hanfland, M.; Wu, S. C.; Shekhar, C.; Sun, Y.; Suss, V.; Schmidt, M.; Schwarz, U.; Pippel, E.; Werner, P.; Hillebrand, R.; Forster, T.; Kampert, E.; Parkin, S.; Cava, R. J.; Felser, C.; Yan, B.; Medvedev, S. A. *Nat. Commun.* **2016**, *7*, 11038.
- (4) Shirodkar, S. N.; Waghmare, U. V. *Phys. Rev. Lett.* **2014**, *112* (15), 157601.
- (5) Chen, X.; Chen, Z.; Li, J. *Chin. Sci. Bull.* **2013**, *58* (14), 1632–1641.
- (6) Franklin, A. D. *Science* **2015**, *349* (6249), aab2750.
- (7) Koppera, R.; Voiry, D.; Yalcin, S. E.; Branch, B.; Gupta, G.; Mohite, A. D.; Chhowalla, M. *Nat. Mater.* **2014**, *13* (12), 1128–34.
- (8) Allain, A.; Kang, J.; Banerjee, K.; Kis, A. *Nat. Mater.* **2015**, *14* (12), 1195–205.
- (9) Eda, G.; Yamaguchi, H.; Voiry, D.; Fujita, T.; Chen, M.; Chhowalla, M. *Nano Lett.* **2011**, *11* (12), 5111–6.
- (10) Wang, L.; Xu, Z.; Wang, W.; Bai, X. *J. Am. Chem. Soc.* **2014**, *136* (18), 6693–7.
- (11) Eda, G.; Fujita, T.; Yamaguchi, H.; Voiry, D.; Chen, M.; Chhowalla, M. *ACS Nano* **2012**, *6* (8), 7311–7317.
- (12) Lin, Y. C.; Dumcenco, D. O.; Huang, Y. S.; Suenaga, K. *Nat. Nanotechnol.* **2014**, *9* (5), 391–6.
- (13) Amara, K. K.; Chen, Y.; Lin, Y.-C.; Kumar, R.; Okunishi, E.; Suenaga, K.; Quek, S. Y.; Eda, G. *Chem. Mater.* **2016**, *28* (7), 2308–2314.
- (14) Song, S.; Keum, D. H.; Cho, S.; Perello, D.; Kim, Y.; Lee, Y. H. *Nano Lett.* **2016**, *16* (1), 188–193.
- (15) Kang, Y.; Najmaei, S.; Liu, Z.; Bao, Y.; Wang, Y.; Zhu, X.; Halas, N. J.; Nordlander, P.; Ajayan, P. M.; Lou, J.; Fang, Z. *Adv. Mater.* **2014**, *26* (37), 6467–6471.
- (16) Lerf, A. *Dalton Trans* **2014**, *43* (27), 10276–91.
- (17) Eknapakul, T.; King, P. D.; Asakawa, M.; Buaphet, P.; He, R. H.; Mo, S. K.; Takagi, H.; Shen, K. M.; Baumberger, F.; Sasagawa, T.; Jungthawan, S.; Meevasana, W. *Nano Lett.* **2014**, *14* (3), 1312–6.
- (18) Janish, M. T.; Carter, C. B. *Scr. Mater.* **2015**, *107*, 22–25.
- (19) Dungey, K. E.; Curtis, M. D.; Penner-Hahn, J. E. *Chem. Mater.* **1998**, *10* (8), 2152–2161.
- (20) Benavente, E.; Santa Ana, M. A.; Mendizábal, F.; González, G. *Coord. Chem. Rev.* **2002**, *224* (1–2), 87–109.
- (21) Charton, S.; Delaunay, F.; Savio, L.; Bernard, F.; Maupoix, C. *Experimental investigation on lithium hydride hydrolysis*; Presented at 16th World Hydrogen Energy Conference, France, 2006.

- (22) Aurbach, D.; Zinigrad, E.; Cohen, Y.; Teller, H. *Solid State Ionics* **2002**, *148* (3–4), 405–416.
- (23) Jeppson, D. W.; Ballif, J. L.; Yuan, W. W.; Chou, B. E. *Lithium literature review: lithium's properties and interactions*; U.S. Department of Energy: Richland, WA, 1978.
- (24) Rhein, R. A. *Lithium Combustion: A Review*; Naval Weapons Center: China Lake, CA, 1990.
- (25) Ishiyama, S.; Baba, Y.; Fujii, R.; Nakamura, M.; Imahori, Y. *Nucl. Instrum. Methods Phys. Res., Sect. B* **2012**, *293*, 42–47.
- (26) Guo, Y.; Sun, D.; Ouyang, B.; Raja, A.; Song, J.; Heinz, T. F.; Brus, L. E. *Nano Lett.* **2015**, *15* (8), 5081–8.
- (27) Lee, C.; Yan, H.; Brus, L. E.; Heinz, T. F.; Hone, J.; Ryu, S. *ACS Nano* **2010**, *4* (5), 2695–2700.
- (28) Hu, T.; Li, R.; Dong, J. *J. Chem. Phys.* **2013**, *139* (17), 174702.
- (29) Julien, C.; Sekine, T.; Balkanski, M. *Solid State Ionics* **1991**, *48* (3–4), 225–229.
- (30) Frey, G. L.; Tenne, R.; Matthews, M. J.; Dresselhaus, M. S.; Dresselhaus, G. *Phys. Rev. B: Condens. Matter Mater. Phys.* **1999**, *60* (4), 2883–2892.
- (31) Chou, S. S.; Sai, N.; Lu, P.; Coker, E. N.; Liu, S.; Artyushkova, K.; Luk, T. S.; Kaehr, B.; Brinker, C. J. *Nat. Commun.* **2015**, *6*, 8311.
- (32) Cheng, Y.; Nie, A.; Zhang, Q.; Gan, L.-Y.; Shahbazian-Yassar, R.; Schwingenschlogl, U. *ACS Nano* **2014**, *8* (11), 11447–11453.
- (33) Zhao, W.; Ghorannevis, Z.; Amara, K. K.; Pang, J. R.; Toh, M.; Zhang, X.; Kloc, C.; Tan, P. H.; Eda, G. *Nanoscale* **2013**, *5* (20), 9677–9683.
- (34) Singh, A.; Shirodkar, S. N.; Waghmare, U. V. *2D Mater.* **2015**, *2* (3), 035013.
- (35) Fohlmeister, L.; Stasch, A. *Aust. J. Chem.* **2015**, *68* (8), 1190–1201.
- (36) Zheng, J.; Zhang, H.; Dong, S.; Liu, Y.; Nai, C. T.; Shin, H. S.; Jeong, H. Y.; Liu, B.; Loh, K. P. *Nat. Commun.* **2014**, *5*, 2995.
- (37) Keum, D. H.; Cho, S.; Kim, J. H.; Choe, D.-H.; Sung, H.-J.; Kan, M.; Kang, H.; Hwang, J.-Y.; Kim, S. W.; Yang, H.; Chang, K. J.; Lee, Y. H. *Nat. Phys.* **2015**, *11* (6), 482–486.
- (38) Guo, H.; Yang, T.; Yamamoto, M.; Zhou, L.; Ishikawa, R.; Ueno, K.; Tsukagoshi, K.; Zhang, Z.; Dresselhaus, M. S.; Saito, R. *Phys. Rev. B: Condens. Matter Mater. Phys.* **2015**, *91* (20), 205415.
- (39) Sun, Y.; Wang, Y.; Sun, D.; Carvalho, B. R.; Read, C. G.; Lee, C. H.; Lin, Z.; Fujisawa, K.; Robinson, J. A.; Crespi, V. H.; Terrones, M.; Schaak, R. E. *Angew. Chem., Int. Ed.* **2016**, *55* (8), 2830–4.
- (40) Cho, S.; Kim, S.; Kim, J. H.; Zhao, J.; Seok, J.; Keum, D. H.; Baik, J.; Choe, D.-H.; Chang, K. J.; Suenaga, K.; Kim, S. W.; Lee, Y. H.; Yang, H. *Science* **2015**, *349* (6248), 625–628.
- (41) Mak, K. F.; Lee, C.; Hone, J.; Shan, J.; Heinz, T. F. *Phys. Rev. Lett.* **2010**, *105* (13), 136805.
- (42) Carvalho, A.; Ribeiro, R. M.; Castro Neto, A. H. *Phys. Rev. B: Condens. Matter Mater. Phys.* **2013**, *88* (11), 115205.
- (43) Wang, Y.; Ou, J. Z.; Chrimes, A. F.; Carey, B. J.; Daeneke, T.; Alsaif, M. M.; Mortazavi, M.; Zhuiykov, S.; Medhekar, N.; Bhaskaran, M.; Friend, J. R.; Strano, M. S.; Kalantar-Zadeh, K. *Nano Lett.* **2015**, *15* (2), 883–90.
- (44) Christodoulides, D. N.; Khoo, I. C.; Salamo, G. J.; Stegeman, G. I.; Van Stryland, E. W. *Adv. Opt. Photonics* **2010**, *2* (1), 60.